Environmental Technology & Innovation 37 (2025) 104032

Contents lists available at ScienceDirect

Environmental Technology & Innovation

journal homepage: www.elsevier.com/locate/eti

Simultaneous sequestration of Cd(II) and Se(IV) by sulfidated nanoscale zerovalent iron impregnated in shrimp shell-derived biochar: Mechanism and site energy distribution analysis

Xin Teng [a,b], Mingyu Wu [a,b], Zhuangzhuang Yue [a], Xingtang Liang [a,*], Zijie Liu [a,*], Shufei Jiao [a], Yanjun Zhang [a], Yanzhen Yin [a]

[a] Guangxi Key Laboratory of Green Chemical Materials and Safety Technology, School of Petroleum and Chemical Engineering, Beibu Gulf University, Qinzhou 535011, China
[b] School of Chemistry and Chemical Engineering, Guangxi University, Nanning 530004, China

ARTICLE INFO

Keywords:
Simultaneous adsorption
Cadmium ion
Selenite
Sulfidated nanoscale zerovalent iron
Shrimp shell-derived biochar
Site energy distribution theory

ABSTRACT

The simultaneous removal of Cd(II) cation and Se(IV) oxoanion from water by adsorption remains a challenge due to their opposite charges. Herein, we impregnate sulfidated nanoscale zerovalent iron into porous shrimp shell-derived biochar to establish Fe(0) and FeS active sites for trapping Se(IV) and Cd(II), respectively. The resulting composite (SNZVI/$BC_{0.3}$) exhibited adsorption capacities of 177.8 and 206.6 mg/g for Cd(II) and Se(IV) in the single-component system, respectively, at an initial pH of 5.0. In the binary system, these values became 128.4 and 282.8 mg/g. Meanwhile, SNZVI/$BC_{0.3}$ could eliminate over 97 % of Se(IV) and 99 % of Cd(II) in real-world water samples with environmental level of these contaminants (1.0 mg/L). In addition, SNZVI/$BC_{0.3}$ reduced the bioavailable content of Se and Cd in waterlogged soil (pH = 6.6) from 2.531 and 4.921 mg/kg to 1.407 and 0.908 mg/kg, respectively. Characterization-based analysis indicated that the reduction of Se(IV) by Fe(0) and the displacement reaction between Fe(II) in FeS and Cd(II) were the main adsorption mechanisms for the Se(IV) and Cd(II) sequestration, respectively. Moreover, site energy distribution analysis supported the synergistic adsorption of Se(IV) and Cd(II) on SNZVI/$BC_{0.3}$ via cation bridges formed by the captured Cd(II), which promoted the Se(IV) sequestration. This work provides a strategy for the simultaneous remediation of Cd(II) and Se(IV) in water and soil.

1. Introduction

Cadmium ion (Cd(II)), a potent environmental contaminant, can lead to osteoporosis and kidney failure at a high intake (Fu et al., 2023). However, some modern industrial practices such as ore mining and metallurgy bring an excessive discharge of Cd(II) into the water environment, posing serious hazards to human beings and ecology (Zhu et al., 2022). In China, Cd(II) is the primary pollution of the agricultural soil, leading to more than 7 % (equivalent to approximately 7.2 $\times 10^6$ ha) of the soil sample exceeding the soil environmental quality limit of China (He et al., 2017). In order to decrease the Cd toxicity in the polluted soil, selenium, especially selenite (Se(IV)) is proposed to be used under a flooding condition, which would lead to a co-existence of Cd(II) and Se(IV) in the

* Corresponding authors.
E-mail addresses: liangxingtang@bbgu.edu.cn (X. Liang), fengye83818@163.com (Z. Liu).

https://doi.org/10.1016/j.eti.2025.104032
Received 22 October 2024; Received in revised form 27 December 2024; Accepted 12 January 2025
Available online 17 January 2025

Fig. 1. Schematic illustration for the SNZVI/BC synthesis.

wastewater (Li et al., 2022). In addition, Se(IV), the most toxic form of the Se species, widely exists in the effluents of mining and metal processing (Xin et al., 2021). Although Se is a vital trace element for animals and humans, it emerges an extremely high toxicity at an elevated concentration(Wang et al., 2022c). Therefore, a strategy for remediating aqueous Cd(II) and Se(IV) is urgently demanded.

Due to the opposite charge, the simultaneous removal of cationic Cd(II) and oxoanionic Se(IV) from water remains challenging, especially in the popular remediation technology, e.g., adsorption. In which, the adsorption performance is significantly pH-dependent, and the cationic metals are preferable to be captured at high pH while the low pH is suitable for the oxoanions adsorption (Ifthikar et al., 2020). Limited literature showed that the bioremediation, using a bacterial consortium from Pb-Zn mine area, could simultaneously eliminate the Cd(II) and Se(IV) from wastewater (Zhang et al., 2022). However, such method struggled against a long contact time (144 h for Se(IV) and 10 h for Cd(II)) and a low removal capacity (less than 10 mg/g).

For the Cd remediation, several strategies such as ion exchange (Zheng et al., 2023), precipitation (Su et al., 2022), adsorption (González-Fernández et al., 2024) and membrane separation (Zhou et al., 2022b) have been developed. Among these methods, adsorption managed by nanoscale zerovalent iron (NZVI) holds promise due to its environmental compatibility and low cost (Falyouna et al., 2022). However, the complexation of NZVI toward Cd(II), the main mechanism of Cd(II) immobilization, is seriously affected by treatment conditions such as solution pH, resulting in an insufficient removal (Zhang et al., 2014). The sulfidation of NZVI (SNZVI) to promote the Cd(II) capture has recently attracted extensive attentions (Guo et al., 2021; Xu et al., 2020c). Because the solubility product constant of CdS is significantly lower than that of FeS (8.0×10^{-27} *vs* 1.6×10^{-19}), the Fe in FeS can be replaced by Cd and forming the long-term stable CdS precipitate, leading to a higher immobilization of SNZVI toward Cd(II) compared to the NZVI (Guo et al., 2021).

In respect to the Se(IV) sequestration, NZVI is a feasible candidate through reductive removal, yet suffers from the passivation of the iron (hydr)oxides shell and the side reactions between NZVI and the reducible species such as water (Zhou et al., 2022a). Sulfide modification is a recommended approach for remedying the defects of NZVI due to the formation of the iron sulfides (e.g., FeS and FeS_2) around the NZVI. On the one hand, the band gap of FeS_x is lower than that of FeO_x, emerging a more facile electron transfer from the Fe(0) core to the targeted contaminant (Garcia et al., 2021). On the other hand, sulfidation promotes the hydrophobicity of NZVI, which mitigates the unwanted reaction between Fe(0) and water (Kansara et al., 2022; Meng et al., 2022).

Taken together, we speculated that the SNZVI could concurrently capture the aqueous Cd(II) and Se(IV) due to its two main components, i.e., FeS and Fe(0). For the former, it can sequestrate Cd(II) via the displacement of Fe in a wide range of solution pH, while the latter can remove Se(IV) through reduction, forming the insoluble Se(0). In addition, numerous studies identified that the impregnation of SNZVI into a biochar could alleviate the agglomeration and the electron loss of SNZVI particles and, thereby boosting its remediation performance (Meng et al., 2022; Wang et al., 2022a). We have incorporated NZVI into the shrimp shell-derived nitrogen-doped biochar (BC) and found that BC significantly increased the reactivity and electron utilization of NZVI for the selenite removal due to its favorable conductivity, high specific surface and buffering effect (Wu et al., 2023). Therefore, SNZVI impregnated in the shrimp shell-derived biochar (SNZVI/BC) was supposed to be a high-efficiency candidate for simultaneously sequestering Cd(II) and Se(IV). However, the synchronous adsorption behavior and the adsorption mechanism of SNZVI/BC toward Cd (II) and Se(IV) remain unknown.

Site energy distribution theory (SEDT) is a powerful approach for the study of complicated adsorption by providing detailed information about the binding energy of the adsorption system, i.e., adsorbent and adsorbate (Hu et al., 2023). SEDT has been successfully employed for analyzing the adsorption behavior of various adsorbents toward metal cations (Wang et al., 2022b), phosphorus (Li et al., 2021), and antibiotics (Wang et al., 2023b). However, the SEDT analysis for the synchronous removal of the oppositely charged metal(loid)s, i.e., Cd(II) and Se(IV) from water remains absent.

In this work, SNZVI was impregnated in the shell-derived porous Biochar. forming a platform (SNZVI/BC) with the adsorption sites of FeS and Fe(0). Such SNZVI/BC was employed to simultaneously trap the Cd(II) cation and Se(IV) oxoanion from water. The main aims of this work were to (1) explore the influence of the feedstock of Fe(III) and S(-II) on the capture of SNZVI/BC toward Cd(II) and Se(IV); (2) estimate the effect of adsorption conditions such as solution pH, contact time and initial adsorbate concentration on the performance of SNZVI/BC for simultaneous sequestration of Cd(II) and Se(IV); (3) provide insights into the mechanism for the simultaneous adsorption of the oppositely charged Cd(II) and Se(IV) onto SNZVI/BC based on the adsorption site energy analysis; (4) evaluate the application potential of SNZVI/BC for remediating the Se(IV) and Cd(II) co-contaminated soil.

2. Materials and methods

2.1. NZVI/BC synthesis

The synthesis process of SNZVI/BC is displayed in Fig. 1. Firstly, the shrimp shell-derived biochar (BC) without calcium carbonate was prepared according to our previous work (Wu et al., 2023). The NZVI/BC was then synthesized according to the previously reported method with some modifications (Han et al., 2017). Typically, a three-necked flask containing 0.5 g of BC and 100 mL of $FeCl_3$ solution (0.018 M) was sonicated for 30 min. 50 mL of $NaBH_4$ solution (0.35 M) was added dropwise into the three-necked flask under nitrogen purging and 300 rpm mechanical stirring. 50 mL of Na_2S solution with different concentrations was subsequently added into the flask under nitrogen purging and mechanically stirred for another 2 h to prepare the SNZVI/BC with various S/Fe dosed molar ratios (e.g., 0, 0.1, 0.3 and 0.7). The synthesized particles were then withdrawn by a magnet, washed with deoxygenated water and deoxygenated ethanol for three times and, freeze-dried for 12 h. The resultant samples were identified as SNZVI/BC_0, SNZVI/$BC_{0.1}$, SNZVI/$BC_{0.3}$ and SNZVI/$BC_{0.7}$, respectively, according to the S/Fe dose. All chemicals and materials used in this work were presented in the supporting information (Text S1).

2.2. Characterizations

The descriptions for characterizations were provided in the supporting information (Text S2).

2.3. Batch adsorption experiments

The batch experiments for adsorption were performed on a ZQWY-200S shaker (Shanghai Zhichu Instrument CO., Ltd.) with a speed of 150 rpm at 25 ± 1 ℃. For pH dependence experiments, 20 mg of SNZVI/BC was mixed with 20 mL of solution containing Cd (II), Se(IV) and, both Cd(II) and Se(IV), respectively, with the initial pH (pH_0) range from 3.0 ± 0.1–6.0 ± 0.1 for wobbling 12 h; the initial concentrations (C_0) of Cd(II) and Se (IV) were set to be 100 mg/L. Herein, the adsorption conducted in the solution with one ion, i.e., Cd(II) or Se(IV), was labeled as the sole system, while the adsorption conducted in the solution with both Cd(II) and Se(IV) was designated the binary system. The kinetics experiments were managed by adding 50 mg of adsorbent into 50 mL Cd(II) and/or Se(IV) solution with a concentration of 100 mg/L and pH_0 5.0 ± 0.1. Aliquots (100 μL) were withdrawn from the treated solution at the prearranged time intervals and percolated through a 0.45 μm membrane. The resultant solutions were employed to determine the Cd (II) and/or Se(IV) concentration. Adsorption isotherms were conducted on the binary system, in which the C_0 for one ion, i.e., Cd(II) or Se(IV) was altered from 5 mg/L to 300 mg/L, while the paired ion was fixed at the C_0 of 0 mg/L, 100 mg/L, and 200 mg/L, respectively. The dose of adsorbent, pH_0, and contact time were set to be 1.0 g/L, 5.0 ± 0.1 and 12 h, respectively. The Cd(II) and Se(IV) concentrations were determined on an Optima 8000 inductively coupled plasma emission spectrometer (ICP-OES, Perkin Elmer). The adsorption capacity (Q, mg/g) was calculated according to Eq. (1):

$$Q = (C_0 - C_e) \quad V/m \tag{1}$$

where C_e (mg/L) denotes the final ion concentration; V (L) and m (g) signify the volume of the treated solution and the mass of adsorbent, respectively. The water sample with 100 mg/L Se(IV) and Cd(II) was spiked by several compounds including NaCl (0.01 M), $NaNO_3$ (0.01 M), $NaSO_4$ (0.01 M), glucose (100 mg/L) and humic acid (100 mg/L) to study the effect of coexisting compounds on the adsorption. The applicability of SNZVI/BC to the real-world sample was assessed in the synthetic wastewaters including lake water and sea water spiked with 1000 μg/L Se(IV) and Cd(II). Adsorption experiments were conducted in duplicate and the mean value of the result was provided.

2.4. Simulation trials for application in waterlogged soil

The soil was collected on the campus of Beibu Gulf University, fully vacuum-dried at 80 °C, pulverized and sieved 0.425 mm sieve. Such soil with negligible bioavailable Cd and Se revealed a cation exchange capacity of 9.57 cmol/kg and a pH of 6.8. To mimic the co-contaminated soil with Cd(II) and Se(IV), 500 g of soil sample was thoroughly mixed with 250 mL of the Cd(II) and Se(IV) concomitant solution (20 mg/L); the mixture was sealed in a 1000 mL beaker and incubated at room temperature for 7 days. The resultant sample was vacuum-dried and pulverized to obtain the polluted soil with Cd and Se concentration of 10 mg/kg. The pH of the polluted soil was tested to be 6.6. Acidic soils are common in southern China and can significantly increase the Cadmium bioavailability of plants, posing health risks to humans due to the intake. For simulating the acidic soil, 50 mL of H_2SO_4 solution (pH = 1.0) was added to the soil (500 g) prior to the blend with Cd(II) and Se(IV). The subsequent procedures were identical to the preparation of the contaminated soil without pH adjustment. Such co-contaminated soil revealed a pH of 4.6.

In order to simulate the immobilization of Cd and Se in the waterlogged soil, 20 g of co-contaminated soil, 20 mL of water and 0.6 g of SNZVI/$BC_{0.3}$ were added into a closed erlenmeyer flask, shaken for 24 h at 50 rpm and 25 ℃. For comparison, the co-contaminated soils without SNZVI/$BC_{0.3}$ addition were conducted in the same procedure and served as control. The resultant sample was centrifuged for 15 min at 5000 rpm to separate the soil and liquid. The Cd and Se in the supernatant liquid were analyzed on the ICP after passing a 0.45 μm membrane. The treated soils were vacuum-dried and pulverized. The bioavailable Cd and Se in soils were determined according to the methods previously reported by Zhang et al. (Zhang et al., 2023) and Zhou et al. (Zhou et al., 2021), respectively, using

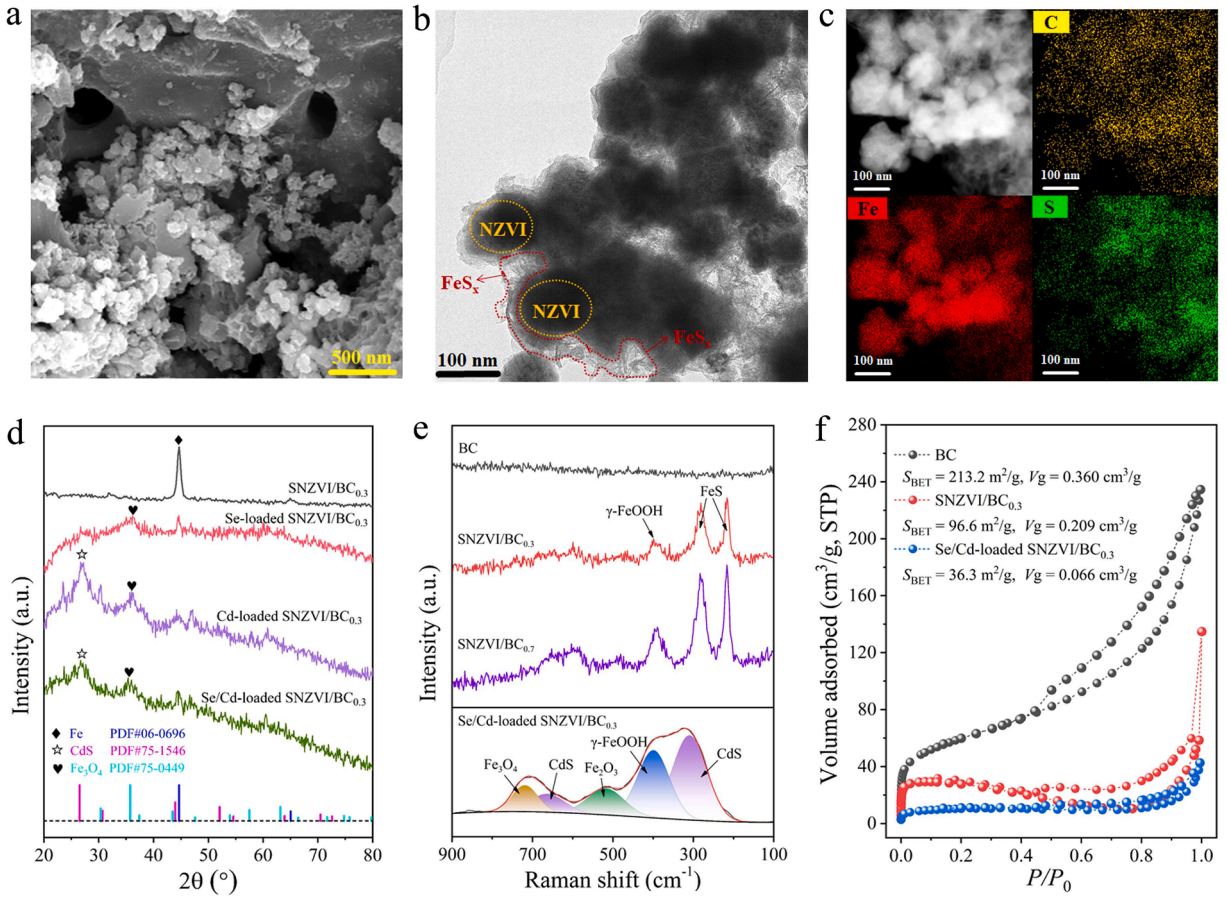

Fig. 2. SEM image of SNZVI/$BC_{0.3}$ (a); TEM image of SNZVI/$BC_{0.3}$ (b); HAADF-STEM elemental mapping for SNZVI/$BC_{0.3}$ (c); XRD patterns for SNZVI/$BC_{0.3}$, Se-loaded SNZVI/$BC_{0.3}$, Cd-loaded SNZVI/$BC_{0.3}$ and Se/Cd-loaded SNZVI/$BC_{0.3}$ (d); Raman spectra for BC, SNZVI/BC of varying S/Fe molar ratios and Se/Cd-loaded SNZVI/$BC_{0.3}$ (e); N_2 sorption isotherms for BC, SNZVI/$BC_{0.3}$ and Se/Cd-loaded SNZVI/$BC_{0.3}$ (f).

ICP.

2.5. Error analysis

The fitting quality of the kinetic model and the isotherm model was evaluated by the adjusted coefficient of determination (Adj. R^2) and root mean square error (RMSE), as expressed in Eq. (2) and Eq. (3), respectively (Hu et al., 2024). In which, y_i, $\hat{y}_i$ and $\bar{y}_i$ represent the observed value, the predicted value and the average of all observations, respectively; n and p denote the number of data points and the number of model parameters, respectively. The curve fitting is configured with a 95 % confidence level.

$$\text{Adj. } R^2 = 1 - \frac{\sum_{i=1}^{n}(y_i - \hat{y}_i)^2}{\sum_{i=1}^{n}(y_i - \bar{y}_i)^2}\left(\frac{n-1}{n-p}\right) \tag{2}$$

$$\text{RMSE} = \sqrt{\frac{1}{n}\sum_{i=1}^{n}(y_i - \hat{y}_i)^2} \tag{3}$$

3. Results and discussion

3.1. Characterization of SNZVI/BC

The successful preparation of SNZVI/BC and the structural feature were demonstrated by SEM, TEM, XRD, XPS and Raman spectroscopy studies. The SEM image of SNZVI/$BC_{0.3}$ indicated the inoculation of numerous particles with irregular shape onto the porous biochar (Fig. 2a). These particles with tens of nanometers were further characterized by TEM and revealed a core-shell morphology, in which the core was suggested to be the NZVI while the lamellar shell was designated as the iron sulfides (Fig. 2b).

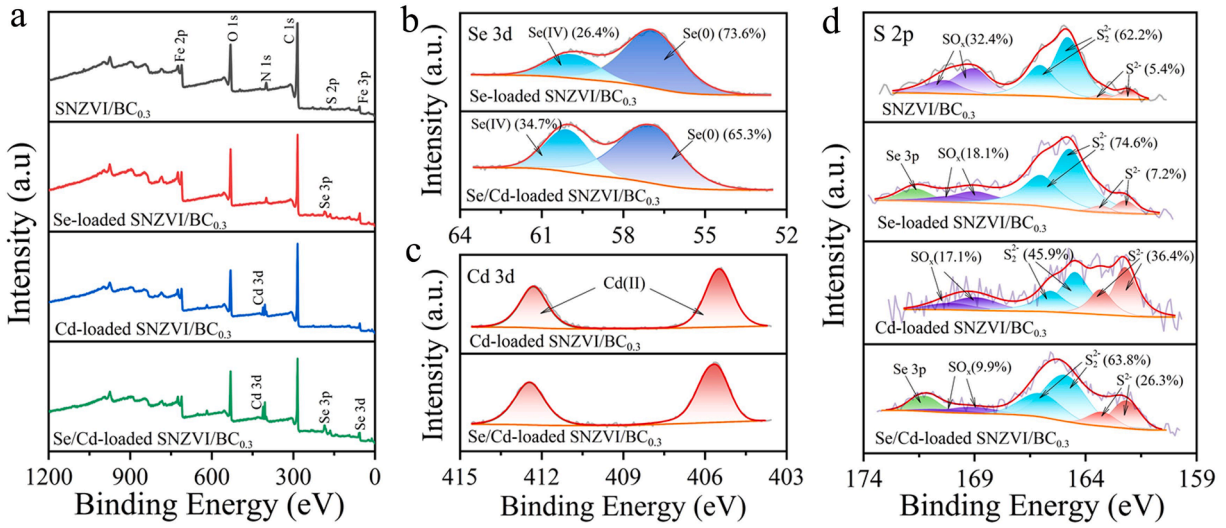

Fig. 3. Full-range XPS spectra of SNZVI/$BC_{0.3}$, Se-loaded SNZVI/$BC_{0.3}$, Cd-loaded SNZVI/$BC_{0.3}$ and Se/Cd-loaded SNZVI/$BC_{0.3}$ (a); Se 3d XPS spectra of Se-loaded SNZVI/$BC_{0.3}$ and Se/Cd-loaded SNZVI/$BC_{0.3}$ (b); Cd 3d XPS spectra of Cd-loaded SNZVI/$BC_{0.3}$ and Se/Cd-loaded SNZVI/$BC_{0.3}$ (c); S 2p XPS spectra for SNZVI/$BC_{0.3}$, Se-loaded SNZVI/$BC_{0.3}$, Cd-loaded SNZVI/$BC_{0.3}$ and Se/Cd-loaded SNZVI/$BC_{0.3}$ (d).

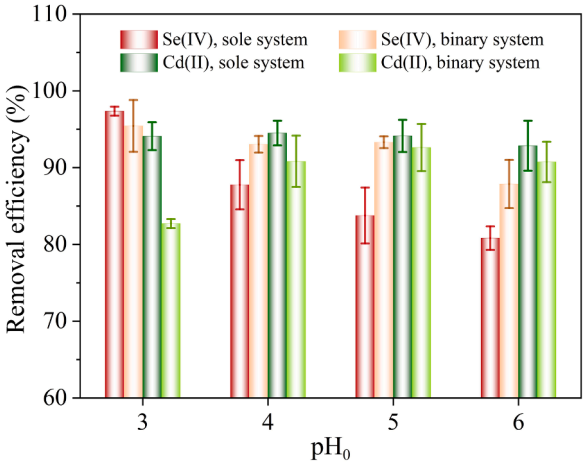

Fig. 4. Effect of initial pH on the removal of Se(IV) and Cd(II) by SNZVI/$BC_{0.3}$ in different systems.

The HAADF-STEM elemental mapping evidenced the homogeneous distribution of sulfur and iron in the particles (Fig. 2c). The XRD pattern of NZVI/$BC_{0.3}$ showed a sharp diffraction peak at $2\theta = 44.7°$, assigning to the Fe(0) (Fig. 2d). The peak intensity was substantially higher than that of NZVI or NZVI/BC (Wu et al., 2023), indicating that the sulfidation upgraded the crystallinity of iron. This result was consistent with the previous studies (Xu et al., 2020a), implying the formation of an alloy compound due to the incorporation of sulfur into the body-centered-cubic structure of Fe(0) (Gao et al., 2023a). Because of the poor crystallinity of iron sulfides (Lv et al., 2019), no characteristic peak for the FeS_x was observed in the XRD pattern.

The Raman spectra of SNZVI/BC exhibited two characteristic bands of lattice and symmetric stretching for Fe-S at about 209 cm^{-1} and 280 cm^{-1}, respectively (Liang et al., 2020), compared with the BC. The intensity of these bands increased as the S/Fe molar ratio increased, suggesting that a higher S/Fe molar ratio promoted the formation of iron sulfides. The XPS full-range spectrum evidenced the elemental composition of SNZVI/BC, i.e., Fe, O, N, C and S (Fig. 3a). The XPS spectrum of S 2p indicated that the S^{2-} and S_2^{2-} were the main form of sulfur on the sample surface and, the oxidized S species (SO_x) was observed due to the oxidation (Fig. 3d). No signal for Fe(0) at about 707.5 eV was observed in the Fe 2p XPS spectrum (Fig. S1), suggesting that the Fe(0) core was coated by the outer layer of iron sulfide. This result is consistent with the TEM analysis. Nitrogen sorption isotherms showed that the incorporation of SNZVI into BC decreased the S_{BET} and V_g from 213.2 m^2/g and 0.360 cm^3/g to 96.6 m^2/g and 0.209 cm^3/g, respectively (Fig. 2f and Fig. S2). Even so, the S_{BET} of SNZVI/$BC_{0.3}$ was significantly higher than that of other SNZVI-based materials, such as S-nZVI (50.3 m^2/g) (Lv et al., 2018), S-nZVI@Kaol (40.6 m^2/g) (Gao et al., 2022). The high surface area would promote the exposure of active sites for capturing Cd(II) and Se(IV).

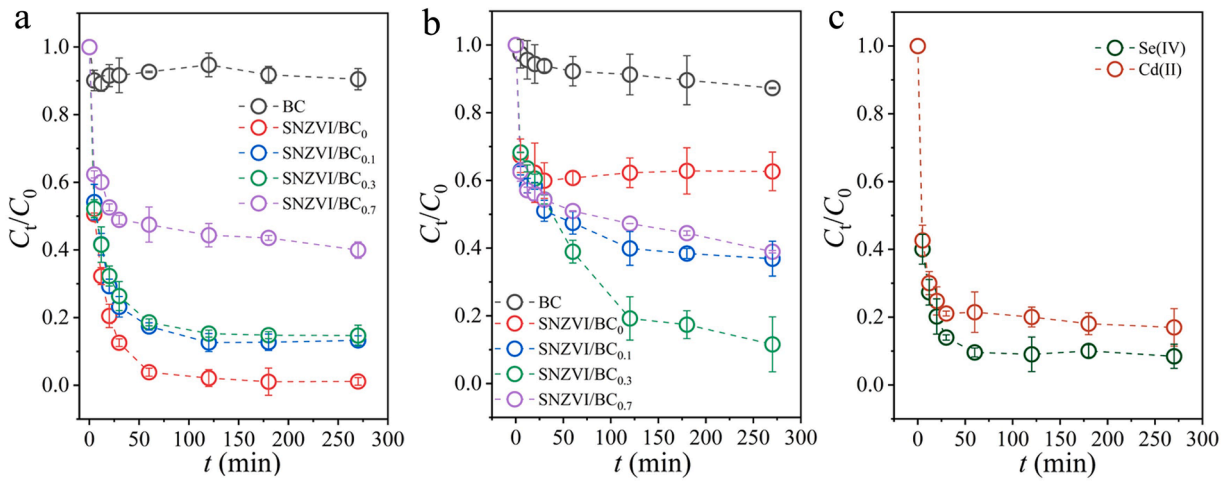

Fig. 5. Se(IV) (a) and Cd(II) (b) adsorption kinetics onto BC and SNZVI/BC with different S/Fe molar ratios in the sole system; Se(IV) and Cd(II) adsorption kinetics onto SNZVI/BC$_{0.3}$ in the binary systems (c).

3.2. Solution pH

Solution pH changes both the surface charge of adsorbent and the species of adsorbate and thereby influences the adsorption performance. Fig. 4 demonstrates the influence of initial solution pH (pH$_0$) on the sequestration performance of SNZVI/BC toward Cd (II) and Se(IV) in different systems. In the sole system of Se(IV), the increase of pH$_0$ significantly diminished the removal efficiency due to the absence of proton for the reduction of Se(IV) ($2Fe^0 + SeO_3^{2-} + 6H^+ \rightarrow 2Fe^{2+} + Se^0 + 3H_2O$). However, in the binary system, the drop of the removal efficiency for Se(IV) was inferior to that in the sole system as the pH$_0$ increased from 3.0 to 6.0, suggesting a higher pH tolerance of SNZVI/BC for Se(IV) uptake in the binary system. In addition, the removal efficiency of Se(IV) in the binary system was greater than that in the Se(IV) sole system at pH$_0$ > 3.0. A likely explanation is that the immobilized Cd(II) on SNZVI/BC acted as new sites for capturing Se(IV).

For the Cd(II) immobilization, the removal efficiency was almost unchanged at the studied pH$_0$ when the adsorption was conducted in the Cd(II) sole system. This result is similar to the sulfidated zero-valent iron for Cd(II) capture (Guo et al., 2021), indicating that the displacement between FeS and Cd(II) is immune to the solution pH. This is different from other adsorbents such as MB2 (Qin et al., 2016), Me-MCS and Ph-MCS (Morshedy et al., 2021), whose adsorptions for Cd(II) were greatly affected by the solution pH. In the binary system, the coexisting Se(IV) decreased the Cd(II) removal efficiency, especially at the low pH$_0$, e.g., pH$_0$ = 3.0. This fall of the Cd(II) removal efficiency might be due to the shelter the formed Se(0) and iron hydroxides, which suppressed the exposure of FeS, the main adsorption site, toward Cd(II) adsorption. In the binary system, the Se(IV) was rapidly reduced to Se(0) that located on the SNZVI/BC surface and partially blocked the contact of FeS toward Cd(II). Besides, the fast elevation of solution pH induced a precipitate of iron hydroxide on the SNZVI/BC surface, which also hindered the exposure of FeS to Cd(II). An acidic condition promoted the reduction of Se(IV), while a high benchmark pH advanced the rise of solution pH (Fig. S3), both of these cases, i.e., the low and high pH conditions, could restrain the uptake of SNZVI/BC toward Cd(II) in the binary system. Therefore, in the binary system, SNZVI/BC presented the highest removal efficiency of Cd(II) at pH$_0$ = 5.0. In which, the Cd(II) removal efficiency was 92.4 %, which was slightly less than the removal efficiency derived from the Cd(II) sole system (94.1 %). However, the Se(IV) removal efficiency in the binary system was significantly higher than that in the sole system (93.1 % *vs* 83.7 %). Therefore, the solution with pH$_0$ = 5.0 was selected for the further experiments.

3.3. Effect of S/Fe molar ratio and adsorption kinetic

The feedstock of S and Fe would change the organization of the two key components, FeS and ZVI, and thereby governed the performance of SNZVI/BC toward Cd(II) and Se(IV) sequestration. Fig. 5a and b show the Se(IV) and Cd(II) removal as the function of contact time by the adsorbents with different S/Fe molar ratios in the sole system, respectively. The BC revealed a significantly lower elimination of Se(IV) and Cd(II) in comparison to the modified BC, i.e., SNZVI/BC, suggesting the key role of zerovalent iron and iron sulfide in the removal of Se(IV) and Cd(II). In the sole system, the Se(IV) removal efficiency decreased as the S/Fe molar ratio increased. This is unlike the utilization of SNZVI to reductively remove the hydrophobic organic contaminants such as tetrabromobisphenol and trichloroethylene (Gao et al., 2023a, 2023b; Gu et al., 2017), in which SNZVI with an appropriate S/Fe composition could promote the removal performance. In our case, Se(IV) is hydrophilic, which would be excluded by the hydrophobic iron sulfide (Xu et al., 2020b), causing an abatement in the sequestration of SNZVI/BC. Furthermore, a high S/Fe molar ratio in the feedstock could decrease the content of NZVI (Song et al., 2017), which also fade the performance of SNZVI/BC toward Se(IV) removal. For the Cd(II) uptake, the NZVI/BC composite revealed a higher removal efficiency than that of BC due to the NZVI, who provided the

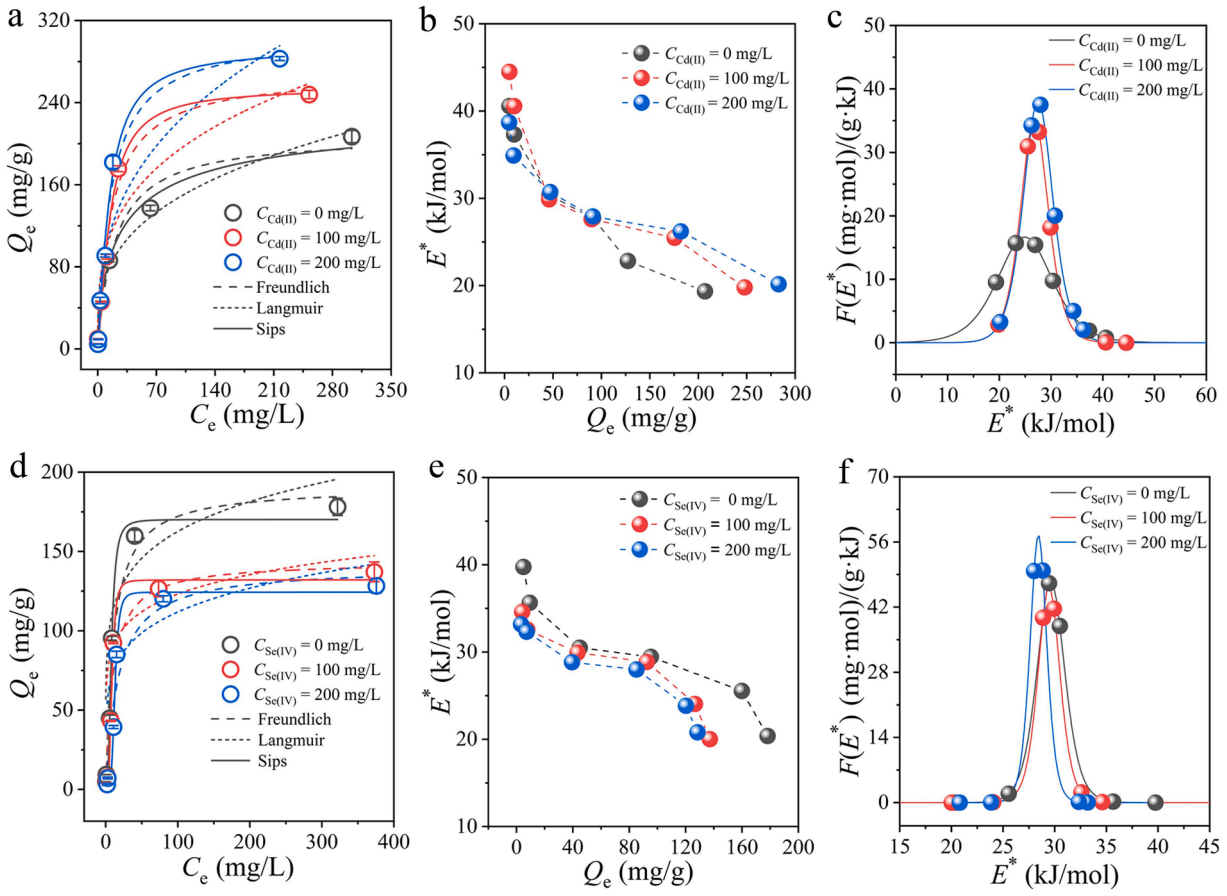

Fig. 6. Comparison of Langmuir, Freundlich, and Sips isotherm models for the Se(IV) (a) and Cd(II) (d) capture by SNZVI/$BC_{0.3}$ in different systems; the approximate adsorption site energy distribution of Se(IV) and Cd(II) derived from Sips isotherm: the plots of E^* *vs* Q_e for Se(IV) (b) and Cd(II) (e) adsorption, the plots of $F(E^*)$ *vs* E^* for Se(IV) (c) and Cd(II) (f) adsorption.

additional adsorption mechanism to Cd(II) (Zhang et al., 2014), such as $\equiv FeOH + Cd^{2+} + H_2O \rightarrow \equiv FeOCdOH + 2H^+$. Meanwhile, the SNZVI/BC with the S/Fe = 0.3 exhibited the maximal removal efficiency. This result is similar to the kaolinite-supported SNZVI for Cd(II) sequestration (Gao et al., 2022), in which the removal efficiency of Cd(II) was promoted as the S/Fe molar ratio increased from 0 to 0.3, but decreased with the further increase of the S/Fe molar ratio. A possible explanation for the drop of Cd(II) uptake at high S/Fe molar ratio is that the excessive iron sulfides blocked the NZVI toward Cd(II) (Li et al., 2017). Evidently, the SNZVI/BC with the S/Fe molar ratio of 0.3 (SNZVI/$BC_{0.3}$) revealed a favorable performance for both the Cd(II) and Se (IV) immobilization and, consequently to be selected for the simultaneous removal of Cd(II) and Se(IV) (Fig. 5c).

Two typical kinetic models, i.e., the pseudo-first-order (PFO) model (Eq. (4)) and the pseudo-second-order (PSO) model (Eq. (5)), were employed to analyze the adsorption of SNZVI/BC toward Se(IV) and Cd(II) (Deng et al., 2024). In which, Q_t (mg/g) assigns the metal uptake at time t (min); Q_1 and Q_2 (mg/g) designate the equilibrium uptake for the PFO and PSO model, respectively; k_1 (l/min) and k_2 (g/(mg·min)) denote the rate constant of the PFO and PSO model, respectively.

$$Q_t = Q_1(1 - e^{-k_1 t}) \quad (4)$$

$$Q_t = Q_2{}^2 \quad k_2 \quad t/(1 + Q_{e2} \quad k_2 \quad t) \quad (5)$$

The fitting results are shown in Fig. S4, and the corresponding parameters are tabulated in Table S1 and Table S2. The SNZVI/BC samples demonstrated a higher correlation coefficient ($R^2 > 0.95$) and a smaller RMSE value for PSO model than that for PFO model in all adsorption systems, identifying that the rate-controlling step was chemisorption (Wang et al., 2023a; Wen and Hu, 2021). Impressively, the SNZVI/BC featured a significantly higher capture rate in the binary system than that in the sole-component system when immobilizing Se(IV) and Cd(II). The k_2 for Cd(II) and Se(IV) uptake in the binary system are 5.81×10^{-3} and 3.75×10^{-3} g/(mg·min), respectively, which are substantially greater than that in the sole-component system (0.51×10^{-3} and 2.50×10^{-3} g/(mg·min) for Cd(II) and Se(IV) uptake, respectively). This result indicated the synergistic effect in the simultaneous sequestration of Cd(II) and Se(IV), that is, the immobilized ion could perform as the active site to attract the other ion with the opposite charge, and thereby promoting the capture rate. This is similar to the simultaneous adsorption of positively charged Cd(II) and negatively charged

Table 1
The parameter in Langmuir, Freundlich and Sips adsorption model of Se (IV) and Cd (II) adsorption on SNZVI/$BC_{0.3}$.

Isotherm model	Constant	Cd(II)			Se(IV)		
		[Se(IV)] 0 mg/L	[Se(IV)] 100 mg/L	[Se(IV)] 200 mg/L	[Cd(II)] 0 mg/L	[Cd(II)] 100 mg/L	[Cd(II)] 200 mg/L
Langmuir	Q_{m1} (mg/g)	190.7	143.7	140.3	208.4	268.9	307.4
	K_l (L/mg)	0.093	0.100	0.058	0.049	0.060	0.062
	R^2	0.971	0.927	0.927	0.963	0.985	0.984
	RMSE	10.51	13.39	12.27	12.48	9.66	11.25
Freundlich	K_f (mg/g)(mg/L)^n	78.7	65.7	48.6	34.5	49.0	43.8
	n	6.34	7.32	5.52	3.145	3.325	2.821
	R^2	0.837	0.825	0.865	0.986	0.910	0.884
	RMSE	43.11	41.25	33.67	7.65	23.1	30.55
Sips	Q_{m2} (mg/g)	170.2	132.1	124.3	237.0	254.3	293.2
	K_s (L/mg)	0.130	0.120	0.079	0.032	0.070	0.072
	b	2.77	3.50	4.59	0.68	1.34	1.27
	R^2	0.985	0.989	0.990	0.990	0.991	0.985
	RMSE	6.47	4.26	3.95	6.29	6.68	9.40

Cr(VI) onto the composite of carboxymethyl cellulose and polyethyleneimine (Song et al., 2020).

3.4. Effect of temperature and adsorbent dosage

The effect of the SNZVI/$BC_{0.3}$ dosage on the simultaneous sequestration of Se(IV) and Cd(II) is shown in Fig. S5. In the two-component system with the $C_0 = 100$ mg/L, the capture capacities of SNZVI/BC for Cd(II) and Se(IV) gradually decreased as the dosage increased. In contrast, the removal efficiency of Cd(II) and Se(IV) increased with the increase of the dosage, and when the dosage was greater than 1.0 g/L, the removal efficiency remained almost constant.

The removal efficiencies of Se(IV) and Cd(II) by SNZVI/$BC_{0.3}$ at different temperatures (25 °C, 35 °C and 45 °C) in the binary system are shown in Fig. S6. The removal efficiency of Se(IV) by SNZVI/$BC_{0.3}$ gradually increased with the rise of temperature, which is similar to our previous work (Wu et al., 2023). Su et al. (2015) showed that the capture of SNZVI toward Cd(II) was an endothermic process, and a high temperature was conducive to the adsorption of Cd(II). However, in this work, the removal efficiency of Cd(II) remained almost unchanged within the studied temperature range. This might be due to the fact that Se(IV) was sequestrated on SNZVI/$BC_{0.3}$ more rapidly than Cd(II), forming a barrier that prevented the exposure of FeS to Cd(II).

3.5. Adsorption isotherm and site energy analysis

The plots of Q_e as a function of C_e at different systems for SNZVI/$BC_{0.3}$ are illustrated in Fig. 6a and d to investigate the interaction of Cd(II) and Se(IV) in the adsorption. For the Se(IV) removal, the coexisting Cd(II) promoted the adsorption capacity of SNZVI/$BC_{0.3}$ toward Se(IV). For example, the Q_e of SNZVI/$BC_{0.3}$ toward Se(IV) was 206.8 mg/g in the sole system with $C_0 = 500$ mg/L, while the Q_e increased to 282.9 mg/g in the binary system with 200 mg/L of Cd(II). However, SNZVI/$BC_{0.3}$ revealed a diminished uptake for Cd(II) as the Se(IV) concentration increased. These results indicated the interaction of Cd(II) and Se(IV) on the surface of SNZVI/$BC_{0.3}$, which will be discussed in the following section. In spite of this, the Q_e of SNZVI/$BC_{0.3}$ toward Cd(II) (178.2 mg/g for the sole system and 128.4 mg/g for the binary system) outperforms the previously reported S-nZVI (85.0 mg/g) (Su et al., 2015). In addition, in both the sole-component or binary-component system, the adsorption performance of SNZVI/$BC_{0.3}$ for Cd(II) and Se(IV) can be comparable to that of the adsorbents reported recently (Table S3).

In order to study the adsorption properties of SNZVI/BC toward Se(IV) and Cd(II) in the sole and binary systems, the equilibrium data of adsorption was examined by using three nonlinear isotherm models, i.e., the Langmuir (Eq. (6)), the Freundlich (Eq. (7)), and the Sips (Eq. (8)) model (Wang et al., 2025; Xu et al., 2021). In which, Q_e, Q_{m1}, and Q_{m2} (mg/g) designate the equilibrium adsorption capacity, theoretical adsorption capacity of Langmuir and Sips isotherm, respectively; K_l (L/mg), K_f ((mg/g)(mg/L)^n), and K_s (L/mg) signify the model constant of Langmuir, Freundlich and Sips, respectively; n and b are the dimensionless constants of Freundlich and Sips model, respectively. Therein, the Sips model denotes a hybrid form of Langmuir and Freundlich model, and b signifies the heterogeneity factor of the adsorbent. The b values approach to 1.0, indicating the homogenous binding sites of adsorbent, while values of b deviate from 1.0, suggesting heterogeneous adsorbents (Ma et al., 2020):

$$Q_e = Q_{m1} K_l C_e / (1 + K_l C_e) \tag{6}$$

$$Q_e = K_f C_e^{\,1/n} \tag{7}$$

$$Q_e = Q_{m2} (K_s C_e)^b / [1 + (K_s C_e)^b] \tag{8}$$

The fitting results and the corresponding parameters are shown in Fig. 6 and Table 1, respectively. Among these isotherm models, the Sips model with the highest correlation coefficient ($R^2 > 0.98$) and the smallest performed the best fit for the sequestration of Se

Table 2
The key parameters of SEDT calculation results based on Sips model.

Parameters	Se(IV)			Cd(II)		
	[Cd(II)] 0 mg/L	[Cd(II)] 100 mg/L	[Cd(II)] 200 mg/L	[Se(IV)] 0 mg/L	[Se(IV)] 100 mg/L	[Se(IV)] 200 mg/L
$\mu(E^*)$ (kJ/mol)	24.91	26.78	27.47	29.62	29.45	28.42
$\sigma(E^*)$ (kJ/mol)	6.34	3.34	3.42	1.69	1.29	0.98

(IV) and Cd(II) onto SNZVI/$BC_{0.3}$ in the studied systems. This result indicated that the adsorption of SNZVI/$BC_{0.3}$ toward Se(IV) and Cd (II) followed the Freundlich model at low concentrations, while it conformed to the Langmuir model at high concentrations (Rajabi et al., 2022). In addition, the b values for all adsorption processes were averted from 1.0, indicating a heterogeneous adsorption site on the SNZVI/$BC_{0.3}$ (Ma et al., 2020; Yang et al., 2024).

In order to further study the adsorption properties of Se(IV) and Cd(II) onto SNZVI/BC, the site energy distribution theory (SEDT) was employed. By combining with the isothermal model, the SEDT can delineate the heterogeneous adsorption on a specific surface from the standpoint of energy and provides the energy of adsorption sites and the relevant distribution function [55]. Generally, the site energy distribution was established by the integral equation (Eq. (9)) based on the theory of heterogeneous surface adsorption (Song et al., 2024):

$$Q_e(C_e) = \int_0^{+\infty} Q_h(E, \quad C_e) \quad F(E)\ dE \tag{9}$$

where $Q_e(C_e)$ (mg/g) is the total adsorption capacity on a specific heterogeneous surface; adsorption energy (E, kJ/mol) symbolizes the difference of adsorption energy between solute and solvent on a certain adsorption site; $Q_h(E, C_e)$ (mg/g) and $F(E)$ (mg·mol/(g·kJ)) signify the energetically homogeneous isotherm and site energy frequency distribution, respectively. According to the Cerofolini approximation, the relationship between equilibrium concentration of adsorbate (C_e, mg/L, Se(IV) and Cd(II) in this word) and E can be formulated as Eq. (10) (Wang et al., 2022b). In which, C_s denotes the saturation concentration of Se(IV) (Se in Na_2SeO_3) and Cd(II) (Cd in $CdCl_2$), and it is gained from the *PubChem* database. T (K) and R (8.314 J/(mol·K)) represent the absolute temperature and the gas constant, respectively. E_s (kJ/mol) designates the adsorption energy at $C_e = C_s$, implying the lowest binding energy for the adsorption. E^* (kJ/mol) signifies the difference of adsorption energies of solute and solvent on the adsorbent surface, using the reference point of E_s. A higher E^* value suggests a more stable adsorption (Chen et al., 2019):

$$C_e = C_s \exp[-(E - E_s)/(R \quad T)] = C_s \exp[-E^*/(R \quad T)] \tag{10}$$

$$F(E^*) = -\mathrm{d}Q_e(E^*)/\mathrm{d}E^* \tag{11}$$

Combining Eq. (9) and Eq. (10), the $F(E^*)$ is acquired by differentiating the $Q_e(E^*)$ isotherm based on the Cerofolini condensation approximation, as expressed in Eq. (11) (Shen et al., 2015). Incorporating the Sips model, the model with the best fit, into Eq. (9), the final form of $F(E^*)$ is presented as Eq. (12).

$$F(E^*) = \frac{Q_{m2}\ \mathrm{b}\ (K_s \quad C_s)^{\mathrm{b}} \quad (R\ T)^{-1} \exp[-\mathrm{b}\ E^*/(R\ T)]}{\{1 + (K_s \quad C_s)^{\mathrm{b}} \exp[-\mathrm{b}\ E^*/(R\ T)]\}^2} \tag{12}$$

In addition, the expectation value ($\mu(E^*)$, kJ/mol) and standard deviation ($\sigma(E^*)$, kJ/mol) for E^* were employed to study the average energy of adsorption site and the surface heterogeneity of site energy, as presented in Eq. (13), Eq. (14) and Eq. (15) (Li et al., 2021; Song et al., 2024), respectively:

$$\mu(E^*) = \int_0^{+\infty} E^* \quad F(E^*) \quad \mathrm{d}E^* \Big/ \int_0^{+\infty} F(E^*)\ \mathrm{d}E^* \tag{13}$$

$$\mu(E^{*2}) = \int_0^{+\infty} E^{*2} \quad F(E^*)\mathrm{d}E^* \Big/ \int_0^{+\infty} F(E^*)\mathrm{d}E^* \tag{14}$$

$$\sigma(E^*) = [\mu(E^{*2}) - \mu(E^*)^2]^{0.5} \tag{15}$$

The plots for E^* *vs* Q_e and $F(E^*)$ *vs* E^* are depicted in Fig. 6, and the corresponding data including $\mu(E^*)$ and $\sigma(E^*)$ are listed in Table 2. SNZVI/$BC_{0.3}$ exhibited a significant drop in E^* as the equilibrium adsorption capacity increased at all studied adsorption systems, indicating that Se(IV) and Cd(II) were firstly captured to the adsorption sites with high-energy and then to the low-energy adsorption sites (He et al., 2019). For the Se(IV) sequestration, especially in the scope with high Q_e, e.g., $Q_e > 100$ mg/g, the E^* increased as the Cd(II) concentration increased, which resulted in a higher average energy of adsorption site ($\mu(E^*)$) (Table 2). This result suggested that the adsorbed Cd(II) on the SNZVI/$BC_{0.3}$ surface promoted the number of high-energy adsorption site, that is, the trapped Cd(II) could act as cation bridges to attach the negatively charged Se(IV) and thereby promoted the adsorption affinity. In addition, the $\sigma(E^*)$ value for Se(IV) adsorption in the binary system was drastically diminished in comparison to the value in the sole system (Table 2), indicating a more homogeneous surface of site energy (Li et al., 2021). Typically, the heat of a chemical reaction is in

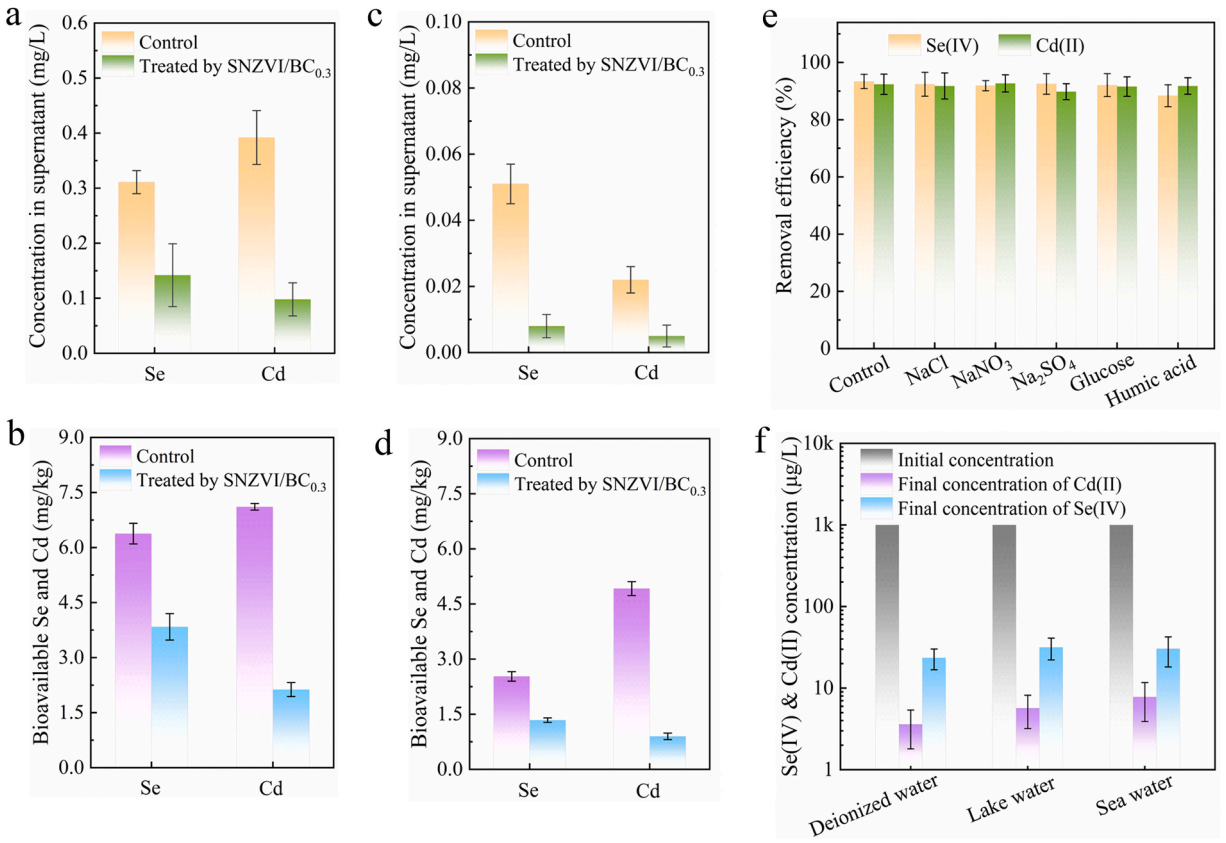

Fig. 7. The concentrations of Se and Cd in supernatant for the soil with pH 4.6 (a) and 6.6 (c) before and after SNZVI/$BC_{0.3}$ treatment; the concentrations of bioavailable Cd and Se for the soil with pH 4.6 (b) and 6.6 (d) before and after SNZVI/$BC_{0.3}$ treatment; Effect of the coexisting compounds on the co-adsorption of Se(IV) and Cd(II) on the SNZVI/$BC_{0.3}$; application of SNZVI/$BC_{0.3}$ for the simultaneous removal of Se(IV) and Cd (II) from deionized, lake and sea water samples spiked with 1000 μg/L Se(IV) and Cd(II).

the range of 21– 420 kJ/mol (Yan et al., 2017). In this work, the $\mu(E^*)$ for Se(IV) adsorption onto SNZVI/$BC_{0.3}$ in different systems were in the 19.35- 44.49 kJ/mol range. Furthermore, the proportion of the adsorption sites with $E^* < 21$ kJ/mol, the sites conducted by physical absorption, was estimated to be 24.8 %, 4.8 %, and 3.9 % for the Se-sole system, binary system with 100 mg/L Cd(II) and binary system with 200 mg/L Cd(II), respectively. These results identified the domination of chemisorption in the Se(IV) sequestration, which is consistent with the kinetic analysis. Meanwhile, they again demonstrated the substitution of the low-energy sites in SNZVI/$BC_{0.3}$ by the trapped Cd(II), a high-energy site, for capturing Se(IV).

For the Cd(II) adsorption, at all studied systems, the E^* ranged from 20.05 to 39.76 kJ/mol, and the proportion of adsorption sites with $E^* < 21$ kJ/mol was less than 0.01 %, substantiating the chemisorption (Yan et al., 2017). The E^* for SNZVI/$BC_{0.3}$ decayed upon the increase of Se(IV) content in the binary system, causing a decrease of the $\mu(E^*)$ (Table 2). Besides, the $\sigma(E^*)$ decreased as the Se (IV) concentration increased, indicating that the trapped Se(IV) on the SNZVI/$BC_{0.3}$ surface promoted the homogeneity of site energy toward Cd(II) adsorption. A possible explanation for these results might be that the immobilized Se, in the form of Se(IV) and/or Se(0), shielded the key adsorption sites, FeS, toward Cd(II) and, thereby inhibited their reaction. In fact, the trapped Se(IV) could attract Cd (II) by electrostatic interaction, while its adsorption affinity was inferior to that of FeS toward Cd(II). This viewpoint could be verified by the following fact. The average site energies of SNZVI/$BC_{0.3}$ toward Se(IV) and Cd(II) capture were 24.91 and 29.62 kJ/mol and these values changed to 27.47 and 28.42 kJ/mol, respectively, in the binary system with 200 mg/L coexisting ion. This result suggested that the reaction heat of Se(IV) and Cd(II) on the SNZVI/$BC_{0.3}$ surface was in the 24.91–29.62 kJ/mol range, lower than the average site energy of SNZVI/$BC_{0.3}$ toward Cd(II) sequestration (29.62 kJ/mol).

3.6. The applicability of SNZVI/$BC_{0.3}$ for Cd(II) and Se(IV) co-immobilization in the real-world samples

To study the applicability of SNZVI/BC in the real-world samples, SNZVI/$BC_{0.3}$ was used to immobilize Se(IV) and Cd(II) in the waterlogged soil. As shown in Fig. 7, Se(IV) and Cd(II) were more easily released from the acidic soil (pH = 4.6) in comparison to the neutral soil (pH = 6.6), resulting in higher concentrations of Se(IV) and Cd(II) in the soil supernatant (0.311 mg/L and 0.392 mg/L at pH = 4.6 *vs* 0.051 mg/L and 0.022 mg/L at pH = 6.6) and higher bioavailable concentrations of Se(IV) and Cd(II) in the soil (6.381 mg/kg and 7.110 mg/kg at pH = 4.6 *vs* 2.531 mg/kg and 4.921 mg/kg at pH = 6.6). SNZVI/$BC_{0.3}$ decreased the Se(IV) and Cd

(II) concentrations of the supernatant of acidic soil from 0.311 mg/L and 0.392 mg/L to 0.153 mg/L and 0.091 mg/L, respectively. Meanwhile, SNZVI/$BC_{0.3}$ diminished the concentration of bioavailable concentrations of Se and Cd in the same soil from 6.381 mg/kg and 7.110 mg/kg to 4.042 mg/kg and 2.206 mg/kg respectively. For the neutral soil, the Se(IV) and Cd(II) concentrations of supernatant were decreased from 0.051 mg/L and 0.022 mg/L to 0.009 mg/L and 0.006 mg/L, respectively, while the bioavailable concentrations of Se and Cd were decreased from 2.531 mg/kg and 4.921 mg/kg to 1.407 mg/kg and 0.908 mg/kg, respectively, after utilizing SNZVI/$BC_{0.3}$. These results indicated a high performance of SNZVI/$BC_{0.3}$ for the sequestration of Se(IV) and Cd(II) in waterlogged soil. Impressively, the immobilization performance of SNZVI/$BC_{0.3}$ for Se(IV) in waterlogged soil was inferior to that for Cd(II), which was different from the result conducted in water. In which, the capture capacity of SNZVI/$BC_{0.3}$ for Se(IV) was higher than that for Cd(II) (Fig. 6a and d). A possible explanation for this might be that the Fe(0) in SNZVI/$BC_{0.3}$, the key component for Se(IV) capture, was partly eliminated by the side reaction with water during the competitive adsorption with soils. However, the FeS was relatively stable and performed well for the Cd(II) immobilization in the waterlogged soil. In the real-world water sample

The effect of the typical coexisting compounds on the simultaneous sequestration of Se(IV) and Cd(II) is shown in Fig. 7e. For the Cd (II) sequestration, SNZVI/$BC_{0.3}$ showed that the removal efficiency for the studied compounds-containing system was comparable to the control. In the humic acid-containing system, because of the competitive adsorption [22], SNZVI/$BC_{0.3}$ revealed a mild decrease in the removal efficiency of Se(IV) compared to the control (88.3 % *vs* 93.4 %). However, the other coexisting compounds exhibited little effect on the Se(IV) sequestration. These results indicated the high tolerance of SNZVI/$BC_{0.3}$ to the coexisting compounds in the co-adsorption of Se(IV) and Cd(II). The applicability of SNZVI/$BC_{0.3}$ for the Se(IV) and Cd(II) sequestration was further studied in the real-world water sample spiked with Se(IV) and Cd(II). As shown in Fig. 7f, SNZVI/$BC_{0.3}$ eliminated over 97 % of Se(IV) and 99 % of Cd (II) from the studied samples, highlighting a great potential of SNZVI/$BC_{0.3}$ for simultaneously sequestrating Se(IV) and Cd(II) from the real-world samples.

3.7. Removal mechanism based on the characterization analysis

The SEM images of spent samples revealed a coating that composed of numerous irregular sheets on the SNZVI/$BC_{0.3}$ (Fig. S7). Such sheets mainly consisted of iron oxides, i.e., Fe_3O_4 and γ-FeOOH, which were derived from the reactions between Fe(0) and oxidants such as Se(IV) and O_2. This viewpoint could be confirmed by the XRD and the Raman spectroscopy studies (Fig. 2e and f). The XRD patterns of the spent SNZVI/$BC_{0.3}$ revealed the diffraction peak of Fe_3O_4 at $2\theta = 36.2°$ compared with the untapped SNZVI/$BC_{0.3}$, along with the disappearance of the Fe(0) diffraction peak. Meanwhile, the diffraction peak ($2\theta = 26.8°$) of CdS emerged in the XRD patterns of the Cd-loaded SNZVI/$BC_{0.3}$ and the Se/Cd-loaded SNZVI/$BC_{0.3}$, supporting the formation of CdS. This result indicated that the substitution reaction between iron sulfides and Cd(II) to form the insoluble CdS was one of the mechanisms for capturing Cd(II). Furthermore, the intensity of the CdS diffraction peak for the spent SNZVI/$BC_{0.3}$ derived from the Cd(II) sole system was higher than that from the binary system (Fig. 2d), suggesting that more CdS was formed in the Cd(II) sole system in comparison to the binary system. This accords with the experimental data (Fig. 5), in which the SNZVI/$BC_{0.3}$ revealed a higher adsorption capacity in the Cd(II) sole system than that in the binary system. In the Raman spectrum of SNZVI/$BC_{0.3}$ after sequestrating Se(IV) and Cd(II) (Fig. 2f), the characteristic peaks of γ-FeOOH, Fe_2O_3, and Fe_3O_4 centered at 398.9 cm^{-1}, 516.5 cm^{-1}, and 719.4 cm^{-1} were observed (Guo et al., 2021). In addition, two peaks ascribed to Cd-S vibration appeared at about 311.4 cm^{-1} and 661.7 cm^{-1} (Guo et al., 2021; Kotkata et al., 2009), along with the disappearance of the characteristic peaks of FeS in the Raman spectrum of the fresh SNZVI/$BC_{0.3}$ (Fig. 2f). These results again evidenced the capture of Cd(II) via the formation of CdS precipitate, in which the Fe in FeS was replaced by Cd(II).

The SNZVI/$BC_{0.3}$ before and after capturing metal ions was characterized by XPS to further explore the removal mechanism (Fig. 3). The full-range XPS spectra of the spent SNZVI/$BC_{0.3}$ conducted in Se(IV) sole system and the binary system identified the Se 3d signal at about 58 eV, while the Cd 3d signal at about 410 eV appeared in the XPS spectra of spent SNZVI/$BC_{0.3}$ derived from the Cd(II) sole system and the binary system, compared with the fresh SNZVI/$BC_{0.3}$ (Fig. 3a). These results indicated the adsorption of Se(IV) and Cd(II) onto SNZVI/$BC_{0.3}$. The Se 3d XPS spectra could be deconvoluted into two sub-peaks at 56.5 eV and 59.6 eV, attributing to the Se (0) and Se(IV), respectively, indicating the partial reduction of the trapped Se(IV) into Se(0) (Wu et al., 2023). The proportion of Se(0) for the Se-loaded SNZVI/$BC_{0.3}$ was higher than that of the Se/Cd-loaded SNZVI/$BC_{0.3}$ (73.6 % *vs* 65.3 %), suggesting that more Se(IV) was reduced by SNZVI/$BC_{0.3}$ in the Se(IV) sole system in comparison to the binary system. However, SNZVI/$BC_{0.3}$ showed a lower adsorption capacity for Se(IV) in the sole system than that in the binary system. A possible explanation for this result might be that the trapped Cd(II) in the binary system acted as new active sites for Se(IV) capture. The Cd 3d XPS spectra for the Cd-loaded SNZVI/$BC_{0.3}$ and the Se/Cd-loaded SNZVI/$BC_{0.3}$ exhibited the same binding energies of Cd(II) at 411.2 eV and 404.5 eV (Lv et al., 2018), indicating the absence of redox reaction in the Cd(II) adsorption onto SNZVI/$BC_{0.3}$. For the S 2p XPS spectra (Fig. 3d), the studied samples presented three types of sulfur, i.e., $\underline{S}O_x$, $\underline{S}_2^{2-}$ and, $\underline{S}^{2-}$ (Brumovsk et al., 2020). The proportion of SO_x decreased after utilization due to the dissolution. The relative amount of $\underline{S}_2^{2-}$ and $\underline{S}^{2-}$ in SNZVI/$BC_{0.3}$ did not change significantly during adsorption in the Se(IV) sole system, suggesting that the redox reaction between Se(IV) and sulfur is negligible. However, the $\underline{S}^{2-}$, as the main site for Cd(II) capture, was exposed in the sequestration of SNZVI/$BC_{0.3}$ toward Cd(II), resulting in a substantial increase in its proportion. The Cd-loaded SNZVI/$BC_{0.3}$ displayed a higher proportion of S^{2-} than that of Se/Cd-loaded SNZVI/$BC_{0.3}$ (36.4 % *vs* 26.3 %), suggesting a superior capture capacity of SNZVI/$BC_{0.3}$ for Cd(II) in the sole system than that in the binary system. This accords with the experimental results.

The evidence and mechanism for adsorption were also studied by the FT-IR, SEM-EDS and N_2 adsorption tests. As shown in Fig. S8, the FT-IR spectra of Se-loaded SNZVI/$BC_{0.3}$ and Se/Cd-loaded SNZVI/$BC_{0.3}$ highlighted the symmetric and antisymmetric stretching of Se-O at 687 cm^{-1} and 842 cm^{-1} (Kolmas et al., 2014), respectively, compared to the fresh SNZVI/$BC_{0.3}$, again evidencing the adsorption of Se(IV). The intensities of the two bands for Se/Cd-loaded SNZVI/$BC_{0.3}$ were significantly greater than that of Se-loaded SNZVI/$BC_{0.3}$, demonstrating a higher absorption capacity of SNZVI/$BC_{0.3}$ for Se(IV) in the binary system. This corresponds to the

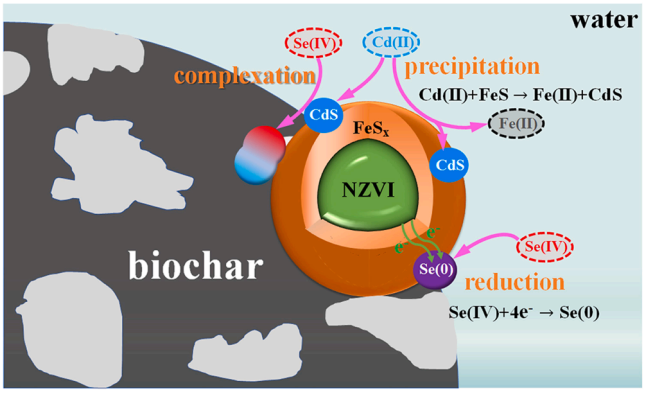

Fig. 8. The possible mechanism for the simultaneous adsorption of Se(IV) and Cd(II) onto SNZVI/BC.

experimental result, suggesting that the trapped Cd(II) in the SNZVI/$BC_{0.3}$ acted as the binding sites for the Se(IV) sequestration. The signals of Se and Cd element were detected in the SEM-EDS element mapping of Se/Cd-loaded SNZVI/$BC_{0.3}$, along with the background elements including C, O, N, Fe and S (Fig. S9), again confirming the adsorption of Se(IV) and Cd(II). In addition, the Se/Cd-loaded SNZVI/$BC_{0.3}$ revealed a higher content of iron on the sample surface than that of the fresh SNZVI/$BC_{0.3}$ (Fig. S10), indicating that the released iron from the SNZVI/$BC_{0.3}$ was precipitated on the SNZVI/$BC_{0.3}$ surface due to the high pH of the treated solution (Fig. S3). Such precipitates filled the pores of the Biochar. causing a significant decrease in the specific surface area and pore volume of the SNZVI/$BC_{0.3}$ (Fig. 2f).

In this paper, zero-valent iron sulfide was constructed on shrimp shell biochar, and Cd(II) and Se(IV) were solidified by FeS and Fe (0), respectively. The interaction of two ions with opposite charges during adsorption was studied. the possible mechanism for the simultaneous removal of Cd(II) cation and Se(IV) oxoanion from water by SNZVI/BC is depicted in Fig. 8. (1) SNZVI/BC adsorbs Cd(II) mainly through the substitution of Cd(II) with Fe(II) in FeS, and adsorbs Se(IV) through the reduction of Fe(0). (2) Cd(II) and Se(IV) interact on the surface of SNZVI/BC, and the adsorbed Cd(II) can promote Se(IV) by using cationic salt bridge to adsorb the negatively charged Se(IV). The adsorbed Se(IV) can adsorb positively charged Cd(II), but the adsorption site energy of the adsorbed Se(IV) on Cd (II) is lower than that of the FeS on Cd(II), and the adsorbed Se(IV) or generated Se(0) partially covers the FeS site, resulting in a small decrease in adsorption capacity.

3.8. Recyclability

In order to study the reusability of SNZVI/$BC_{0.3}$ for the simultaneous sequestration of Se(IV) and Cd(II), SNZVI/$BC_{0.3}$ (0.05 g) was used to treat the Se(IV) and Cd(II) solution (50 mL, C_0 = 50 mg/L, pH_0 = 5.0, contact time = 6.0 h). The spent SNZVI/$BC_{0.3}$ was withdrawn by a magnet. Such SNZVI/$BC_{0.3}$ was then treated by NaOH solution (0.1 M) and HCl solution (0.05 M) to discharge adsorbed Se(IV) and Cd(II), respectively. The regenerated SNZVI/$BC_{0.3}$ was used for the next co-adsorption of Se(IV) and Cd(II). Four cycles of adsorption-desorption were carried out to evaluate the reusability of SNZVI/$BC_{0.3}$, and the results are shown in Fig. S11. After four cycles of adsorption-desorption, the removal efficiency of Se(IV) and Cd(II) by SNZVI/$BC_{0.3}$ decreased from 96.4 % and 94.1–62.8 % and 43.7 %, respectively. The decrease in the removal efficiency of Se(IV) and Cd(II) was mainly due to the irreversible consumption of the active component Fe(0) and the dissolution of FeS, respectively.

4. Conclusions

In summary, sulfidated nanoscale zerovalent iron was impregnated into the shrimp shell-derived Biochar. forming a biochar-based platform (SNZVI/BC) with FeS and Fe(0). Such SNZVI/BC could trap Cd(II) cation and Se(IV) oxoanion from water and waterlogged soil due to the displacement reaction between Fe(II) in FeS and Cd(II) and the reduction of Se(IV) by Fe(0). The SNZVI/BC with a feedstock of S/Fe = 0.3 (molar ratio) presented an excellent performance for simultaneously sequestrating Cd(II) and Se(IV). The SNZVI/$BC_{0.3}$ featured a synergistic effect on the simultaneous adsorption of Cd(II) and Se(IV), revealing a substantially faster adsorption rate and a higher pH tolerance in the binary system than it did in the sole system. The trapped Cd(II) on the SNZVI/$BC_{0.3}$ acted as new sites for Se(IV) capture in the binary system and boosted the Se(IV) adsorption compared with the sole system; while the Cd(II) sequestration capacity in the binary system was slightly decreased by the blocker of the generated Se(0) and iron hydroxide in comparison to the sole system. The site energy distribution analysis demonstrated that the chemisorption was dominated in the adsorption of Cd(II) and Se(IV) onto SNZVI/$BC_{0.3}$. The trapped Cd(II) increased the adsorption site energy of SNZVI/$BC_{0.3}$ toward Se (IV), while the Se(IV) adsorption decreased the site energy for Cd(II) sequestration. Both adsorbed ions, i.e., Cd(II) and Se(IV) could promote the homogeneity of site energy of SNZVI/$BC_{0.3}$ for the counter ion capture. This work presented an alternative to simultaneously decontaminate metal cation and oxoanion. Moreover, the methodologies for investigating the simultaneous adsorption behavior of the oppositely charged adsorbate could be transferred to the extended systems of water treatment.

CRediT authorship contribution statement

Zhuangzhuang Yue: Resources. **Xingtang Liang:** Writing – review & editing, Formal analysis. **Xin Teng:** Writing – original draft, Methodology, Data curation. **Mingyu Wu:** Methodology, Investigation. **Yanzhen Yin:** Writing – review & editing, Supervision. **Shufei Jiao:** Investigation. **Yanjun Zhang:** Software, Resources. **Zijie Liu:** Software, Project administration.

Declaration of Competing Interest

The authors declare that they have no known competing financial interests or personal relationships that could have appeared to influence the work reported in this paper.

Acknowledgments

This work was supported by the National Natural Science Foundation of China (Grant No. 52060001). The authors acknowledged the counterpart aid project for discipline construction from Guangxi University (Grant No. 2023B04).

Appendix A. Supporting information

Supplementary data associated with this article can be found in the online version at doi:10.1016/j.eti.2025.104032.

Data availability

Data will be made available on request.

References

Brumovsk, M., Filip, J., Malina, O., Oborná, Jana, Sracek, O., Reichenauer, T.G., Andrsková, Pavlína, Zboil, R., 2020. Core-shell Fe/FeS nanoparticles with controlled shell thickness for enhanced trichloroethylene removal. ACS Appl. Mater. Interfaces 12 (31), 35424–35434. https://doi.org/10.1021/acsami.0c08626.

Chen, Z., Ma, W., Lu, G., Meng, F., Duan, S., 2019. Adsorption of levofloxacin onto mechanochemistry treated zeolite: modeling and site energy distribution analysis. Sep. Purif. Technol. 222, 30–34. https://doi.org/10.1016/j.seppur.2019.04.010.

Deng, S., Liu, Y., Guo, C., Zhou, X., Lu, Q., Fan, Z., Gao, Z., Xiang, Q., Jin, Z., Chen, X., 2024. Polyvinyl chloride microplastics reduce Cd(II) adsorption and enhance desorption with soil-dependent mechanisms. Environ. Technol. Inno. 34, 103607. https://doi.org/10.1016/j.eti.2024.103607.

Falyouna, O., Maamoun, I., Bensaida, K., Tahara, A., Sugihara, Y., Eljamal, O., 2022. Encapsulation of iron nanoparticles with magnesium hydroxide shell for remarkable removal of ciprofloxacin from contaminated water. J. Colloid Interf. Sci. 605, 813–827. https://doi.org/10.1016/j.jcis.2021.07.154.

Fu, P., Wang, X., Shi, J., Zhou, L., Hou, Q., Wang, W., Tian, Y., Qin, J., Bi, W., Liu, F., 2023. Enhanced removal of As(III) and Cd(II) from wastewater by alkali-modified Schwertmannite@Biochar. Environ. Technol. Inno. 31, 103197. https://doi.org/10.1016/j.eti.2023.103197.

Gao, F., Zhang, M., Yang, X., Ahmad, S., Tang, J., 2023b. Post-sulfidation of biochar supported nanoscale zero-valent iron with different sulfur precursors: reactivity and selectivity on tetrabromobisphenol A reduction. Chem. Eng. J. 461, 141953. https://doi.org/10.1016/j.cej.2023.141953.

Gao, F., Lyu, H., Ahmad, S., Xu, S., Tang, J., 2023a. Enhanced reductive degradation of tetrabromobisphenol A by biochar supported sulfidated nanoscale zero-valent iron: Selectivity and core reactivity. Appl. Catal. B Environ. 324, 122246. https://doi.org/10.1016/j.apcatb.2022.122246.

Gao, R., Hu, P., Dai, Y., Zhang, Y., Liu, L., Yang, W., 2022. Removal of cadmium (II) from aqueous solutions by a novel sulfide-modified nanoscale zero-valent iron supported on kaolinite: treatment efficiency, kinetics and mechanisms. Appl. Surf. Sci. 602, 154353. https://doi.org/10.1016/j.apsusc.2022.154353.

Garcia, A.N., Zhang, Y., Ghoshal, S., He, F., O'Carroll, D.M., 2021. Recent advances in sulfidated zerovalent iron for contaminant transformation. Environ. Sci. Technol. 55 (13), 8464–8483. https://doi.org/10.1021/acs.est.1c01251.

González-Fernández, L.A., Medellín-Castillo, N.A., Navarro-Frómeta, A.E., Castillo-Ramos, V., Sánchez-Polo, M., Carrasco-Marín, F., 2024. Optimization of hydrochar synthesis conditions for enhanced Cd(II) and Pb(II) adsorption in mono and multimetallic systems. Environ. Res. 261, 119651. https://doi.org/10.1016/j.envres.2024.119651.

Gu, Y., Wang, B., He, F., Bradley, M.J., Tratnyek, P.G., 2017. Mechanochemically sulfidated microscale zero valent iron: pathways, kinetics, mechanism, and efficiency of trichloroethylene dechlorination. Environ. Sci. Technol. 51 (21), 12653–12662. https://doi.org/10.1021/acs.est.7b03604.

Guo, Y., Li, X., Liang, L., Lin, Z., Su, X., Zhang, W., 2021. Immobilization of cadmium in contaminated soils using sulfidated nanoscale zero-valent iron: effectiveness and remediation mechanism. J. Hazard. Mater. 420, 126605. https://doi.org/10.1016/j.jhazmat.2021.126605.

Han, Lu, Chen, Yun, Ouyang, Da, Yan, Jingchun, Qian, Linbo, 2017. Nanoscale zero-valent iron supported by biochars produced at different temperatures: synthesis mechanism and effect on Cr(VI) removal. Environ. Pollut. https://doi.org/10.1016/j.envpol.2016.12.077.

He, J., Guo, J., Zhou, Q., Yang, J., Fang, F., Huang, Y., 2019. Analysis of 17α-ethinylestradiol and bisphenol A adsorption on anthracite surfaces by site energy distribution. Chemosphere 216, 59–68. https://doi.org/10.1016/j.chemosphere.2018.10.136.

He, Y., Huang, D., Zhu, Q., Wang, S., Liu, S., He, H., Zhu, H., Xu, C., 2017. A three-season field study on the in-situ remediation of Cd-contaminated paddy soil using lime, two industrial by-products, and a low-Cd-accumulation rice cultivar. Ecotox. Environl. Safe. 136, 135–141. https://doi.org/10.1016/j.ecoenv.2016.11.005.

Hu, Q., Lan, R., He, L., Liu, H., Pei, X., 2023. A critical review of adsorption isotherm models for aqueous contaminants: curve characteristics, site energy distribution and common controversies. J. Environ. Manag. 329, 117104. https://doi.org/10.1016/j.jenvman.2022.117104.

Hu, Q., Pei, Q., Zhang, Y., Pang, S., Feng, C., 2024. Facile preparation of oxygen vacancy-rich magnesium oxide for advanced removal of phosphate from aqueous solutions. J. Water Process Eng. 66, 2214–7144. https://doi.org/10.1016/j.jwpe.2024.106080.

Ifthikar, J., Shahib, I.I., Sellaoui, L., Jawad, A., Zhao, M., Chen, Z., Chen, Z., 2020. pH tunable anionic and cationic heavy metal reduction coupled adsorption by thiol cross-linked composite: physicochemical interpretations and fixed-bed column mathematical model study. Chem. Eng. J. 401, 126041. https://doi.org/10.1016/j.cej.2020.126041.

Kansara, K., Bolan, S., Radhakrishnan, D., Palanisami, T., Al-Muhtaseb, Aa.H., Bolan, N., Vinu, A., Kumar, A., Karakoti, A., 2022. A critical review on the role of abiotic factors on the transformation, environmental identity and toxicity of engineered nanomaterials in aquatic environment. Environl. Pollut. 296, 118726. https://doi.org/10.1016/j.envpol.2021.118726.

Kolmas, J., Oledzka, E., Sobczak, M., Na??Cz-Jawecki, G., 2014. Nanocrystalline hydroxyapatite doped with selenium oxyanions: a new material for potential biomedical applications. Mater. Sci. Eng. C. Mater. Biol. Appl. 39, 134–142. https://doi.org/10.1016/j.msec.2014.02.018.
Kotkata, M.F., Masoud, A.E., Mohamed, M.B., Mahmoud, E.A., 2009. Synthesis and structural characterization of CdS nanoparticles. Phys. E 41 (8), 1457–1465. https://doi.org/10.1016/j.physe.2009.04.020.
Li, D., Zhou, C., Wu, Y., An, Q., Zhang, J., Fang, Y., Li, J.Q., Pan, C., 2022. Nanoselenium integrates soil-pepper plant homeostasis by recruiting rhizosphere-beneficial microbiomes and allocating signaling molecule levels under Cd stress. J. Hazard. Mater. 432, 128763. https://doi.org/10.1016/j.jhazmat.2022.128763.
Li, H., Zhao, Y., Xiao, Z., Yang, M., Zhou, B., 2021. Analysis on approximate site energy distribution and adsorption behaviors unveils reasons for highly efficient phosphorus removal by a novel sludge-based magnetic gel bead. Chem. Eng. J. 422, 130028. https://doi.org/10.1016/j.cej.2021.130028.
Li, J., Zhang, X., Sun, Y., Liang, L., Pan, B., Zhang, W., Guan, X., 2017. Advances in sulfidation of zerovalent iron for water decontamination. Environ. Sci. Technol. 51 (23), 13533–13544. https://doi.org/10.1021/acs.est.7b02695.
Liang, L., Li, X., Lin, Z., Tian, C., Guo, Y., 2020. The removal of Cd by sulfidated nanoscale zero-valent iron: the structural, chemical bonding evolution and the reaction kinetics. Chem. Eng. J. 382, 122933. https://doi.org/10.1016/j.cej.2019.122933.
Lv, D., Zhou, X., Zhou, J., Liu, Y., Li, Y., Yang, K., Lou, Z., Baig, S.A., Wu, D., Xu, X., 2018. Design and characterization of sulfide-modified nanoscale zerovalent iron for cadmium (II) removal from aqueous solutions. Appl. Surf. Sci. 442, 114–123. https://doi.org/10.1016/j.apsusc.2018.02.085.
Lv, D., Zhou, J., Cao, Z., Xu, J., Liu, Y., Li, Y., Yang, K., Lou, Z., Lou, L., Xu, X., 2019. Mechanism and influence factors of chromium (VI) removal by sulfide-modified nanoscale zerovalent iron. Chemosphere 224, 306–315. https://doi.org/10.1016/j.chemosphere.2019.02.109.
Ma, J., Zhou, B., Zhang, H., Zhang, W., 2020. Fe/S modified sludge-based biochar for tetracycline removal from water. Powder Technol. 364, 889–900. https://doi.org/10.1016/j.powtec.2019.10.107.
Meng, Y., Chen, X., Ai, D., Wei, T., Fan, Z., Wang, B., 2022. Sulfur-doped zero-valent iron supported on biochar for tetracycline adsorption and removal. J. Clean. Prod. 379, 134769. https://doi.org/10.1016/j.jclepro.2022.134769.
Morshedy, A.S., Galhoum, A.A., Aleem, A.A.H.A., El-din, M.T.S., Okaba, D.M., Mostafa, M.S., Mira, H.I., Yang, Z., Ibrahim, E., 2021. Functionalized aminophosphonate chitosan-magnetic nanocomposites for Cd (II) removal from aqueous solutions: performance and mechanisms of sorption. Appl. Surf. Sci. 561, 150069. https://doi.org/10.1016/j.apsusc.2021.150069.
Qin, X., Zhou, J., Huang, A., Guan, J., Zhang, Q., Huang, Z., Hu, H., Zhang, Y., Yang, M., Wu, J., 2016. A green technology for the synthesis of cellulose succinate for efficient adsorption of Cd (II) and Pb (II) ions. RSC Adv. 6 (32), 26817–26825. https://doi.org/10.1039/C5RA27280G.
Rajabi, M., Keihankhadiv, S., Suhas, Tyagi, I., Karri, R., Chaudhary, M., Mubarak, N.M., Chaudhary, S., Kumar, P., Singh, P., 2022. Comparison and interpretation of isotherm models for the adsorption of dyes, proteins, antibiotics, pesticides and heavy metal ions on different nanomaterials and non-nano materials—a comprehensive review. J. Nanostructure Chem. 13 43–65. https://doi.org/10.1007/s40097-022-00509-x.
Shen, X., Guo, X., Zhang, M., Tao, S., Wang, X., 2015. Sorption mechanisms of organic compounds by carbonaceous materials: site energy distribution consideration. Environ. Sci. Technol. 49 (8), 4894. https://doi.org/10.1021/es506034e.
Song, G., Fan, W., Zhang, J., Xue, T., Shi, Y., Sun, Y., Ding, G., 2024. Adsorption of anionic dyes from aqueous solutions by a novel CTAB/MXene/carbon nanotube composite: characterization, experiments, and theoretical analysis. Appl. Surf. Sci. 661, 160036. https://doi.org/10.1016/j.apsusc.2024.160036.
Song, L., Feng, Y., Zhu, C., Liu, F., Li, A., 2020. Enhanced synergistic removal of Cr (VI) and Cd (II) with bi-functional biomass-based composites. J. Hazard. Mater. 388, 121776. https://doi.org/10.1016/j.jhazmat.2019.121776.
Song, S., Su, Y., Adeleye, A.S., Zhang, Y., Zhou, X., 2017. Optimal design and characterization of sulfide-modified nanoscale zerovalent iron for diclofenac removal. Appl. Catal. B Environ. 201, 211–220. https://doi.org/10.1016/j.apcatb.2016.07.055.
Su, Q., Xie, Y., Chen, M., Xue, X., Cui, X., 2022. Enhance the removal and immobilization of Cd (II) by the synthesis in situ of dithiocarbamate-geopolymer microsphere composite. J. Colloid Interf. Sci. 622, 562–576. https://doi.org/10.1016/j.jcis.2022.04.069.
Su, Y., Adeleye, A.S., Keller, A.A., Huang, Y., Dai, C., Zhou, X., Zhang, Y., 2015. Magnetic sulfide-modified nanoscale zerovalent iron (S-nZVI) for dissolved metal ion removal. Water Res 74, 47–57. https://doi.org/10.1016/j.watres.2015.02.004.
Wang, A., Hou, J., Feng, Y., Wu, J., Miao, L., 2022a. Removal of tetracycline by biochar-supported biogenetic sulfidated zero valent iron: kinetics, pathways and mechanism. Water Res 225, 119168. https://doi.org/10.1016/j.watres.2022.119168.
Wang, B., Shang, C., Xie, H., Sun, H., Zhang, Q., Xue, L., Tack, F.M.G., Hou, D., Feng, Y., Rinklebe, J., 2022b. Unraveling natural aging-induced properties change of sludge-derived hydrochar and enhanced cadmium sorption site heterogeneity. Biochar 4 (1), 1–20. https://doi.org/10.1007/s42773-022-00159-w.
Wang, H., Yang, Q., Li, Z., Xie, Y., Kong, F., Liang, D., Xia, C., Huang, H., Li, J., Meng, Z., 2023b. Adsorption of antibiotics on montmorillonite and site energy distribution analysis. J. Mol. Liq. 383, 122078. https://doi.org/10.1016/j.molliq.2023.122078.
Wang, H., Wang, S., Wang, S., Fu, L., Zhang, L., 2023a. The one-step synthesis of a novel metal–organic frameworks for efficient and selective removal of Cr (VI) and Pb (II) from wastewater: Kinetics, thermodynamics and adsorption mechanisms. J. Colloid Interf. Sci. 640, 230–245. https://doi.org/10.1016/j.jcis.2023.02.108.
Wang, W., Jiang, R., Lin, C., Wang, L., Liu, Y., Lin, H., 2022c. Multivariate statistical analysis of potentially toxic elements in the sediments of Quanzhou Bay, China: spatial relationships, ecological toxicity and sources identification. Environ. Res. 213, 113750. https://doi.org/10.1016/j.envres.2022.113750.
Wang, X., Wang, B., Liu, Y., Wang, J., Cheng, J.J., Daroch, M., Liu, K.K., 2025. A highly efficient adsorbent adapting to low pH condition for Pb(II) sequestration from aqueous solution − marine diatom: Laboratory and pilot scale tests. Sep. Purif. Technol. 353, 128321. https://doi.org/10.1016/j.seppur.2024.128321.
Wen, J., Hu, X., 2021. Metal selectivity and effects of co-existing ions on the removal of Cd, Cu, Ni, and Cr by ZIF-8-EGCG nanoparticles. J. Colloid Interf. Sci. 589, 578–586. https://doi.org/10.1016/j.jcis.2021.01.021.
Wu, M., Teng, X., Liang, X., Zhang, Y., Huang, Z., Yin, Y., 2023. Supporting nanoscale zero-valent iron onto shrimp shell-derived N-doped biochar to boost its reactivity and electron utilization for selenite sequestration. Chemosphere 319, 137979. https://doi.org/10.1016/j.chemosphere.2023.137979.
Xin, Y., Gu, P., Long, H., Meng, M., Yaseen, M., Su, H., 2021. Fabrication of ferrihydrite-loaded magnetic sugar cane bagasse charcoal adsorbent for the adsorptive removal of selenite from aqueous solution. Colloid Surf. A 614, 126131. https://doi.org/10.1016/j.colsurfa.2020.126131.
Xu, H., Hu, X., Chen, Y., Li, Y., Zhang, R., Tang, C., Hu, X., 2021. Cd(II) and Pb(II) absorbed on humic acid-iron-pillared bentonite: kinetics, thermodynamics and mechanism of adsorption. Colloid Surf. A 612, 126005. https://doi.org/10.1016/j.colsurfa.2020.126005.
Xu, J., Avellan, A., Li, H., Liu, X., Noël, V., Lou, Z., Wang, Y., Kaegi, R., Henkelman, G., Lowry, G.V., 2020b. Sulfur loading and speciation control the hydrophobicity, electron transfer, reactivity, and selectivity of sulfidized nanoscale zerovalent iron. Adv. Mater. 32 (17), 1906910. https://doi.org/10.1002/adma.201906910.
Xu, J., Avellan, A., Li, H., Clark, E.A., Henkelman, G., Kaegi, Rl, Lowry, G.V., 2020a. Iron and sulfur precursors affect crystalline structure, speciation, and reactivity of sulfidized nanoscale zerovalent iron. Environ. Sci. Technol. 54 (20), 13294–13303. https://doi.org/10.1021/acs.est.0c03879.
Xu, W., Hu, X., Lou, Y., Jiang, X., Shi, K., Tong, Y., Xu, X., Shen, C., Hu, B., Lou, L., 2020c. Effects of environmental factors on the removal of heavy metals by sulfide-modified nanoscale zerovalent iron. Environ. Res. 187, 109662. https://doi.org/10.1016/j.envres.2020.109662.
Yan, B., Niu, C., Wang, J., 2017. Analyses of levofloxacin adsorption on pretreated barley straw with respect to temperature: kinetics, π-π electron-donor-acceptor interaction and site energy distribution. Environ. Sci. Technol. 122 (14), 128. https://doi.org/10.1021/acs.est.7b00327.
Yang, L., Li, Y., Chen, D., Gao, J., Shu, S., Pu, X., Yang, H., Tang, J., 2024. Efficient cooperative extraction uranium (VI) from aqueous solution and seawater by a novel phosphate/amidoxime chitosan-based adsorbent. J. Water Process Eng. 61, 105197. https://doi.org/10.1016/j.jwpe.2024.105197.
Zhang, X., Wang, L., Zeng, T., Liu, Y., Wang, G., Liu, J., Wang, A., 2022. The removal of selenite and cadmium by immobilized biospheres: efficiency, mechanisms and bacterial community. Environ. Res. 211, 113025. https://doi.org/10.1016/j.envres.2022.113025.
Zhang, Y., Li, Y., Dai, C., Zhou, X., Zhang, W., 2014. Sequestration of Cd (II) with nanoscale zero-valent iron (nZVI): characterization and test in a two-stage system. Chem. Eng. J. 244 218–226. https://doi.org/10.1016/j.cej.2014.01.061.
Zhang, Y., Li, A., Liu, L., Duan, X., Ge, W., Liu, C., Qiu, G., 2023. Enhanced remediation of cadmium-polluted soil and water using facilely prepared MnO2-coated rice husk biomass. Chem. Eng. J. 457, 141311. https://doi.org/10.1016/j.cej.2023.141311.
Zheng, X., Wu, Q., Huang, C., Wang, P., Cheng, H., Sun, C., Zhu, J., Xu, H., Ouyang, K., Guo, J., Liu, Z., 2023. Synergistic effect and mechanism of Cd(II) and As(III) adsorption by biochar supported sulfide nanoscale zero-valent iron. Environ. Res. 231, 116080. https://doi.org/10.1016/j.envres.2023.116080.

Zhou, F., Li, Y., Ma, Y., Peng, Q., Cui, Z., Liu, Y., Wang, M., Zhai, H., Zhang, N., Liang, D., 2021. Selenium bioaccessibility in native seleniferous soil and associated plants: comparison between in vitro assays and chemical extraction methods. Sci. Total Environ. 762, 143119. https://doi.org/10.1016/j.scitotenv.2020.143119.

Zhou, L., Li, Z., Yi, Y., Tsang, E.P., Fang, Z., 2022a. Increasing the electron selectivity of nanoscale zero-valent iron in environmental remediation: a review. J. Hazard. Mater. 421, 126709. https://doi.org/10.1016/j.jhazmat.2021.126709.

Zhou, W., Wu, P., Zhang, L., Yao, S., Zhu, D., Cai, Y., 2022b. Layer-by-layer assembly of nanocomposite interlayers on a kaolin substrate for enhancing membrane performance of Pb(II) and Cd(II) removal. Sci. Total Environ. 820, 153149. https://doi.org/10.1016/j.scitotenv.2022.153149.

Zhu, Z., Yang, Y., Fan, Y., Zhang, L., Tang, S., Zhu, Y., Zhou, X., 2022. Strontium-doped hydroxyapatite as an efficient adsorbent for Cd(II) removal from wastewater: performance, kinetics, and mechanism. Environ. Technol. Inno. 28, 102575. https://doi.org/10.1016/j.eti.2022.102575.